

Ablation behaviour of ultra-high temperature ceramic matrix composites

Silvestroni, Laura; Vinci, Antonio; Failla, Simone; Zoli, Luca; Rubio Diaz, Virtudes; Binner, Jon; Sciti, Diletta

DOI:

[10.1016/j.jeurceramsoc.2019.03.031](https://doi.org/10.1016/j.jeurceramsoc.2019.03.031)

License:

Creative Commons: Attribution-NonCommercial-NoDerivs (CC BY-NC-ND)

Document Version

Peer reviewed version

Citation for published version (Harvard):

Silvestroni, L, Vinci, A, Failla, S, Zoli, L, Rubio Diaz, V, Binner, J & Sciti, D 2019, 'Ablation behaviour of ultra-high temperature ceramic matrix composites: role of MeSi₂ addition', *Journal of the European Ceramic Society*, vol. 39, no. 9, pp. 2771-2781. <https://doi.org/10.1016/j.jeurceramsoc.2019.03.031>

[Link to publication on Research at Birmingham portal](#)

Publisher Rights Statement:

Silvestroni, L. et al (2019) Ablation behaviour of ultra-high temperature ceramic matrix composites: role of MeSi₂ addition, Journal of the European Ceramic Society, 39(9), 2771-2781; <https://doi.org/10.1016/j.jeurceramsoc.2019.03.031>

General rights

Unless a licence is specified above, all rights (including copyright and moral rights) in this document are retained by the authors and/or the copyright holders. The express permission of the copyright holder must be obtained for any use of this material other than for purposes permitted by law.

- Users may freely distribute the URL that is used to identify this publication.
- Users may download and/or print one copy of the publication from the University of Birmingham research portal for the purpose of private study or non-commercial research.
- User may use extracts from the document in line with the concept of 'fair dealing' under the Copyright, Designs and Patents Act 1988 (?)
- Users may not further distribute the material nor use it for the purposes of commercial gain.

Where a licence is displayed above, please note the terms and conditions of the licence govern your use of this document.

When citing, please reference the published version.

Take down policy

While the University of Birmingham exercises care and attention in making items available there are rare occasions when an item has been uploaded in error or has been deemed to be commercially or otherwise sensitive.

If you believe that this is the case for this document, please contact UBIRA@lists.bham.ac.uk providing details and we will remove access to the work immediately and investigate.

Ablation behaviour of ultra-high temperature ceramic matrix composites: role of MeSi_2 addition

L. Silvestroni^{1*}, A. Vinci¹, S. Failla¹, L. Zoli¹, V. Rubio², J. Binner², D. Sciti¹

¹*CNR-ISTEC, National Research Council of Italy - Institute of Science and Technology for Ceramics, Via Granarolo 64, I-48018 Faenza, Italy*

²*School of Metallurgy and Materials, University of Birmingham, B15 2TT, Birmingham, UK*

ABSTRACT

A new class of ZrB_2 composites reinforced with 40 vol% C short fibers and containing 5 wt% SiC in combination with 5 wt% MoSi_2 , HfSi_2 or WSi_2 successfully withstood extreme conditions in a oxyacetylene torch. Different responses to the torch testing were recorded depending on which secondary phase was present; this was primarily a result of the final density which ranged between 83 and 94% of the theoretical value. The temperatures achieved on the surfaces of the samples tested also varied as a function of the residual porosity and ranged from 2080 to 2240°C. HfSi_2 additions offered the best performance and exceeded that of the baseline material that contained only SiC. It is believed that this was due to its ability to promote the elimination of porosity during densification and to the refractory nature of its oxide, HfO_2 . In contrast, MoSi_2 and WSi_2 formed highly volatile oxides on the surface, which did not offer better protection than the $\text{ZrO}_2\text{-SiO}_2$ scale that developed in the baseline.

Keywords: Ultra-high temperature ceramics; Ceramic matrix composites; Carbon fiber; microstructure; ablation resistance.

* Corresponding author: L. Silvestroni
Tel. +39 546 699723
Fax. +39 546 46381
e-mail. laura.silvestroni@istec.cnr.it

1. Introduction

Structural materials possessing thermo-mechanical properties capable of withstanding extreme conditions are always of great interest for civil and military aerospace applications. Among the most difficult to achieve are high temperature strength, toughness and oxidation resistance, especially simultaneously in the same material. The EU-funded project C3HARME [<https://c3harme.eu/>] aims to combine the best features of ceramic matrix composites, CMCs, i.e. mechanical reliability, with those of ultra-high temperature ceramics, UHTCs, which impart ablation resistance, with the goal of designing, developing, manufacturing and testing a new class of structural materials with self-healing (SH) capabilities. These are the ultra-high temperature ceramic matrix composites (UHTCMCs). Potential applications for these new materials are propulsion nozzles and thermal protection systems (TPSs) for Earth re-entry or hypersonic flights, in particular near-zero erosion nozzle inserts and near-zero ablation tiles. The materials being developed consist of a matrix based on zirconium diboride (ZrB_2), which offers a balance between cost, mass and high temperature performance, and a reinforcing phase based on continuous or short randomly oriented SiC [1][2][3][4][5][6] or C fibers [7,8,9].

As far as the mechanical properties of these UHTCMCs containing large volume fractions of carbon fiber, i.e. above 30 vol%, are concerned, adequate values have been achieved in terms of strength and toughness, ranging from 300-500 MPa and $6-10 \text{ MPa m}^{1/2}$ [10,11,12,13], respectively. However, to date their high temperature ablative behavior has been poorly explored [14,15,16,17,18], although it is a key requirement for use in harsh environments. Previous experiments on a novel Cf-rich ZrB_2 composite, machined as a throat insert and integrated into a De Laval nozzle composed of converging and diverging graphite parts, demonstrated the capability of such ceramics to resist successfully the effect of a supersonic flame produced by a high velocity oxy-fuel (HVOF) torch test under a mixture of methane, oxygen and air at high temperatures and heat fluxes [8]. The ablation behavior under highly oxidative flames and extreme temperatures also now needs to be verified.

Since both the boride matrix and the Cf reinforcement undergo oxidation above 800°C, it can be desirable to include a protective third phase to increase the level of protection. In this context, silicon carbide (SiC) has largely demonstrated its positive effect on boride-based composites at intermediate temperatures as a result of the formation of a borosilicate glass during oxidation at high temperatures [19,20]. However, above 1650°C and at low oxygen partial pressure, SiC undergoes active oxidation leading to the formation of a SiC-depleted layer, which weakens the material by creating a layered architecture containing pores and voids [21], the amount of which depends on the size, amount and distribution of the SiC phase [21,22].

Other compounds that are able to slow down the oxidation process include the transition metal silicides, MeSi_2 , which also provide a silica-based glass upon oxidation [23,24]. In addition, they can act as sintering aids, enabling the development of dense, fine and refractory microstructures [4,25,26]. In particular, it has recently been determined that MeSi_2 has a key impact on the oxidation behavior of monolithic ZrB_2 ceramics via the modification of the chemistry and nature of the glassy, vapor and crystalline phases formed. This can result in relatively effective sub-layers depending on the temperature ranges encountered [26,27,28].

In this work, ZrB_2 composites were produced containing high volumes, 40 vol%, of short carbon fiber plus 10 vol% of oxidation retardant phases. The latter consisted of 5 vol% of SiC combined with 5 vol% of one of three different MeSi_2 compounds, viz. MoSi_2 , HfSi_2 or WSi_2 . The selection of these silicides was based on their compatibility with high-temperature environments, i.e. they offer melting points above 1600°C, high stiffness and, owing to their beneficial effects on densification, high temperature strength and potential oxidation resistance improvement for borides [23,25,26,27,28]. Additionally, a comparative material without MeSi_2 but containing the same total amount of SH additives, i.e. 10 vol% SiC, was also prepared as a reference baseline. The question posed by this work was whether the replacement of 5 vol% of SiC with 5 vol% of MeSi_2 would significantly improve the ablation resistance. Thus the UHTCMCs were exposed to the flame of an oxyacetylene torch (OAT) at temperatures above 2000°C for 60 s. The analysis of the as-sintered

and oxidized materials is presented and discussed, with the focus being on the effect of the secondary phases in promoting the formation of an ablation resistant microstructure.

The novelty of this work lies in the production and successful testing of a new class of UHTCMCs that can survive extreme conditions of oxidation at up to 2000°C.

2. Experimental procedure

2.1 Materials preparation

The characteristics of the precursor materials, ZrB₂, SiC, MoSi₂, HfSi₂, WSi₂ and carbon fibers, are listed in Table I. The nominal compositions were set as follows (in vol%):

(ZrB ₂ + 10 SiC) + 40 Cf	(ZBS)
(ZrB ₂ + 5 SiC + 5 MoSi ₂) + 40 Cf	(ZBM)
(ZrB ₂ + 5 SiC + 5 HfSi ₂) + 40 Cf	(ZBH)
(ZrB ₂ + 5 SiC + 5 WSi ₂) + 40 Cf	(ZBW)

To enable a good dispersion of the additives, the ceramic powders were initially mixed by wet ball-milling for 4 hours, using SiC milling media in EtOH, then the chopped carbon fibers were added to the slurry and mixed for an additional 20 hours. The slurries were dried in a rotary evaporator and de-agglomerated. Hot-pressing cycles were conducted for all of the different materials in a low vacuum (~100 Pa) using an induction-heated graphite die with an uniaxial pressure of 30 MPa during the heating phase, this was increased to 40 MPa once the sintering temperature of 1900°C was reached. After 30 min at this temperature, the furnace power was turned off and the specimens were allowed to cool naturally.

2.2 Oxyacetylene torch (OAT) tests

Discs of 30 mm diameter and 4 mm height were cut by EDM from the sintered pellets and tested in a custom built oxyacetylene torch facility at the University of Birmingham, UK, Figure 1. The samples were clamped during the test using screws and a holder made of G348 ultra-fine grain

isostatic graphite (Tokai Carbon Europe, Warley, UK) oriented at 90° to the torch flame direction at a distance of 30 mm to achieve a heat flux of 8.5 MW m⁻². The samples were exposed for 60 s to the oxidizing flame with an acetylene: oxygen ratio of 1: 1.35. At the end of the testing period, the samples were gradually moved away from the flame to avoid cracking due to thermal shock. The back face temperature was recorded using a K type thermocouple connected to a data logger and placed in contact with the sample through a hole drilled in the sample holder. A thermal imaging camera (FLIR A655sc, SLIR systems AB, Sweden) and 2-color pyrometer (METIS M3, Sensortherm, Germany) logged the sample surface temperature as a function of time. The 2-color pyrometer (2-CP) was capable of recording temperatures from 1000 to 3000°C and the modified thermal imaging camera (TIC) could record temperatures up to 2800°C when combined with a neutral density filter.

2.3 Characterization

The bulk densities of the sintered pellets were measured by Archimedes' method using distilled water as the liquid medium.

The microstructure before and after each torch test was analyzed on the surface and cross-section using scanning electron microscopy (FE-SEM, Carl Zeiss Sigma NTS GmbH, Oberkochen, DE) and energy dispersive x-ray spectroscopy (EDS, INCA Energy 300, Oxford instruments, UK). The thickness of the oxide layer formed was measured in the center of the disc, i.e. in the area most damaged by the flame.

The topological characterization of the as-machined and oxidized surfaces was performed with a Contour GT-K 3D non-contact profilometer (Bruker, Germany) on areas of 6 x 24 mm² at the center of each disc and the data was analyzed using commercial software (Vision64 Map). The evaluation of texture was undertaken using 3D field parameters since they can provide more comprehensive information about surface texture than 2D data. By definition, the former are less sensitive to individual perturbations and so more stable results are generally obtained. The

evaluation of 3D texture parameters was performed on the datasets collected after de-noising (median filter 5×5) after removing and filtering with an aerial robust gaussian L-filter.

The 4-pt bending flexural strength (σ) of the as-sintered composites was measured at room temperature and at 1500°C in a partially protective argon atmosphere according to the guidelines of the European standards for advanced ceramics EN 843-1 and ENV 820-1 by fracturing five chamfered bars with dimensions of 25 mm x 2.5 mm x 2 mm (length by width by thickness, respectively). A semi-articulated alumina 4-pt fixture (lower span 20 mm, upper span 10 mm) was used in a screw-driven load frame (Instron mod. 1195) with a 1 mm/min cross-head speed.

Phase stability diagrams were computed by means of the commercial package HSC Chemistry v. 6.1 (Outokumpu Research Oy, Pori, Finland).

3. Results and Discussion

3.1 Microstructure and properties of as-sintered materials

The most important parameters affecting the oxidation behavior of Cf-reinforced materials are primarily the density, i.e. the degree of porosity and whether it is connected or not, and the nature and type of secondary phases. Therefore these will be the main focus of the results and discussion, Table 2.

Despite the high volume fiber content, all the materials were observed to have their carbon fibers well dispersed since no agglomeration or macro defects were detected. As confirmation of this, both the linear and surface average roughnesses of the as-machined samples, Ra_0 and Sa_0 , were not significantly different, Table 3.. An example of the microstructure of a ZBS sample is shown in Figure 2a. The fiber length was significantly reduced during processing from the initial 3000 μm to around 150-200 μm as a consequence of the ball milling. Microstructural details of the silicide-containing composites are shown at higher magnification in Figures 2b-d.

The relative density of the Cf-reinforced composites reported in Table 2 is expressed as the percentage ratio of the experimental and theoretical values, the latter being calculated using the rule

of mixtures for the starting compositions. The relative densities were higher than 90% for the ZBS, ZBM and ZBH materials, but only 83.5% for the ZBW. It should be noted that the values for individual samples underwent slight variations due to some significant reactions between the matrix and the sintering additives and reinforcement, as explained later.

The baseline material, ZBS (not shown at high magnification), revealed homogeneously scattered SiC particles and about 7 vol% of residual porosity as determined by image analysis, in agreement with Archimedes' measurements.

For the silicide-containing composites, independent of the MeSi_2 used, the original ZrB_2 grains of the matrix were surrounded by a solid solution with general formula $(\text{Zr},\text{Me})\text{B}_2$, in agreement with previous studies [25,27,28] and as a consequence of the densification process involving a transient liquid phase formed by partial dissociation of the silicide [25]. This feature is particularly visible in ZBH, Figure 2c, owing to a higher amount of Me, in this case Hf, being dissolved in the ZrB_2 lattice. ~10 at% of Hf dissolved due to its similarity with Zr compared to only ~6 and 2 at% for the other two materials, ZBM and ZBW respectively. In all cases, the SiC particles, with dark contrast, were homogeneously scattered through the matrix. In addition, further tiny SiC particles formed at the fiber/matrix interface as a consequence of the silicide dissociation within the hot pressing chamber, resulting in fibers with irregular profile. The material sintered with HfSi_2 (ZBH), which resulted in the greatest degree of densification of the three, displayed reaction products at the fiber edges, see the inset in Figure 2c. These tiny HfC crystals formed locally as a consequence of a Hf-Si-C-B liquid phase running along the fibers during sintering [29].

As for the secondary phases, occasionally MoSi_2 or MoB phase could be detected in the ZBM, whilst residuals of Hf-Si and W-B-C phases were found in ZBH and ZBW, respectively; these are recognizable from the bright contrast in Figures 2b-d.

The room temperature 4-point bending strength, summarized in Table 2, was in the range of similar materials containing high volume fractions of carbon fiber [8] and generally followed the density trend spanning from ~100 MPa for the most porous ZBW to 136 MPa for the most dense

ZBS and ZBH. The strength at 1500°C increased for the two composites available for testing, probably due to partial oxidation of the Si-containing species into healing silica glass. Unfortunately for ZBS and ZBH no bars could be machined and mechanically tested.

3.2 Oxidation behavior under OAT testing

The temperature at the front and back surfaces of the composites was monitored by both TIC and 2-CP and, generally, the 2-color pyrometer measured temperatures very slightly higher than the infra-red camera, see Figure 3a. The plot in Figure 3b displays the thermal profiles of the three materials measured by 2-CP on the front surface. Although the samples were all tested 30 mm from the torch nozzle, and hence saw the same heat flux of 8.5 MW m^{-2} , the heating rate achieved and final maximum temperature achieved on the front and back surfaces varied. The most probable cause was the varying thermal conductivities of the different composites, which were, in turn, related to the residual porosities and compositions. The thickness of the oxide layer that grew during testing will also have had an effect. The ZBW achieved 2240°C, ZBM 2170°C, ZBH 2105°C and the reference ZBS a slightly lower temperature of 2076°C. This is consistent with the lower density samples achieving higher temperatures because they have a lower thermal conductivity and so the heat cannot escape from the front face so easily. The mass of the samples was also monitored before and after OAT testing. The specific weight loss shows the same trend as the porosity and maximum front face temperatures for the silicide-containing materials, highest for ZBW, followed by ZBM and ZBH, Table 2. This indicates a lower oxidation resistance for the samples with higher porosity as expected, due to easier penetration of the oxygen through the pores during the tests. It should be noted, though, that for materials with comparable volume fractions of residual porosity, 7% for the ZBS and 6% for ZBH, different mass losses were observed. The specific mass loss for the ZBH was approximately half that of the ZBS even though it experienced a 30°C hotter temperature, suggesting that the presence of the HfSi₂ improved the oxidation resistance.

3.3 Microstructure of oxidized composites and evolution mechanism

Images of the discs before, during and after torch testing are shown in Figure 4. They all reveal a damaged circular area, with relative extension varying from 6.0 to 8.6% of the total surface disc, as measured by image analysis, and their aspect reflects the temperatures experienced. The ZBS and ZBH were the least damaged, whilst that containing MoSi₂, which attained a 60°C higher temperature, shows the first signs of oxide cracking, and the sample with WSi₂, which achieved 2240°C, some 164°C higher than the reference, displayed some oxide spallation. As a rule of thumb, the whiter regions, i.e. the inner damaged circle, was composed of crystalline ZrO₂, whilst the darker colored regions, i.e. the periphery, contain the silica-based glass, as explained in detail below.

The surface roughness of the oxidized discs is reported in Table 3, whilst Figure 5 shows the topography maps of the silicide-containing materials for a more immediate and straightforward comparison. Sa and Sq are the lowest for ZBS and ZBH and equally high for ZBM and ZBW, in agreement with the appearance of the discs. The topographic images in Figure 5 reflect the degree of damage that the discs underwent and show a more homogeneous surface in the case of ZBS and ZBH, the formation of craters and bubbles in the case of ZBM, and exploded craters with some ablated material in the case of ZBW. The circumference segments identifiable in ZBS and ZBH mark the edges of the hottest zone directly hit by the torch.

All the disc surfaces were depleted of Cf after the torch tests with the central regions composed of only ZrO₂-based crystalline phases, Figure 6a, Figure 7a, Figure 8a and Figure 9a, whilst outside the hottest zone a SiO₂-based glass filled the locations where the fibers had been since they constituted the easiest interconnected channels for fluid flow, Figure 6e, Figure 7d, Figure 8d and Figure 9d. In the case of ZBM, ZBH and ZBW, no clear evidence of Mo, Hf or W was found in the silica glass, as confirmed by the EDS spectra in Figure 7e, Figure 8e and Figure 9e. The ZrO₂ grain morphology also followed a common behavior; in the center the grains were

coarse, partially coalesced or even melted, whilst around the edge they had a granular aspect and retained a very fine microstructure, compare, for example, Figure 6c&f. In addition, in all cases, small cracks departed from the centers towards the less damaged edges. For the ZBM and ZBW, bubbling, fissures and spallation were also clearly visible in the center, see as an example the insets of Figure 7a and Figure 9a, whilst the surface of ZBH was smoother, consistent with the respective temperatures experienced. In addition, in the ZBH, it was possible to identify the oxidation product of the initial $(\text{Zr},\text{Hf})\text{B}_2$ solid solution of the matrix; the ZrO_2 grains were decorated and interpenetrated by stable HfO_2 nano-inclusions, Figure 8c. For the other two silicide-based materials, no inclusions were observed within the outermost ZrO_2 grains owing to the highly volatile nature of the corresponding metal oxides [30,31]. As confirmation of the escape of volatile species, ZrO_2 grains in ZBM show intragranular porosity, Figure 7b&c. It should also be noted that the tiny bright particles visible in ZBW in Figure 9b&c were observed on the surface upon spallation of a small portion of the outermost scale, i.e. in the first sublayers. According to the high volatility of WO_x phases [31], and in agreement with oxidation studies at 1650°C [27], it is presumed that any W-phase that experienced the oxidizing flux at the high temperature of the torch immediately vaporized, leaving effectively pure ZrO_2 grains behind.

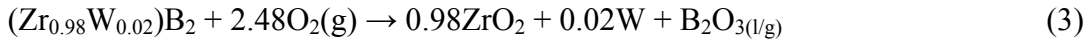
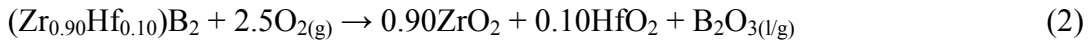
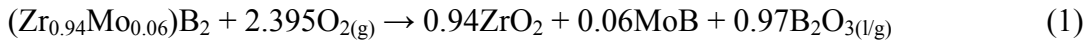
As far as the secondary phases were concerned, no Mo-compound could be detected on the surface of sample ZBM, while Hf-Si residuals oxidized into HfO_2 , Figure 8b, and W-B-C into a WO_3 intergranular phase, Figure 9b, were found on the surface of samples ZBH and ZBW respectively.

Comparative sections of the oxidized discs are shown in Figure 10. The total oxide scale in the centre of each disc, the most damaged areas, was quite homogeneous in thickness but varied depending on the temperature experienced and the silicide added, $95 \pm 2 \mu\text{m}$ for ZBS, $125 \pm 6 \mu\text{m}$ for ZBM, $40 \pm 3 \mu\text{m}$ for ZBH and $>122 \pm 6 \mu\text{m}$ for ZBW. For the latter, no precise measurement of the oxide thickness was possible owing to partial removal of the outer scale. For all systems, no C fibers were found in the ZrO_2 -based scale layer, all the fibers were completely vaporized leaving

just their empty cavities partially filled with silica and other MeSi_2 oxidation products. Undamaged carbon fibers existed only where the boride matrix was found to remain un-oxidized.

For the baseline composite, Figure 11, no SiC particles were found in the ZrO_2 scale, but rather, close to the unoxidized bulk, silica glass filled the voids left by the fiber preferential consumption, whilst moving towards the surface, their cavities were left empty, owing to SiO vaporization, see Figure 11b&c.

For the materials containing MeSi_2 , the $(\text{Zr},\text{Me})\text{B}_2$ solid solutions of the matrices oxidized following the typical oxidation behavior recently outlined in dedicated studies [27,28] and expressed by reactions (1-3), resulting in ZrO_2 grains trapping nano-inclusions based on MoB , HfO_2 and W/WO_3 , depending on the most stable phase at the oxide/boride partial pressure locally established in the sub-surface scales [28], as explained later.



Details of the cross section of the ZBM disc are shown in Figure 12. The oxide layer, partially spalled off upon fracture, is delineated by a dotted line in Figure 12a. Figure 12b-d show the carbon fiber-depleted sites partially filled with silica and MoO_3 , both oxidation products of the MoSi_2 phase according to reaction (4).



When the MoSi_2 was in good contact within the oxidizing boride matrix, the formation of MoB was the most favorable product according to reaction (5). In Figure 12e it is indeed possible to identify the oxidation products of the initial $(\text{Zr},\text{Mo})\text{B}_2$ solid solution composed of ZrO_2 grains encasing MoB nano-inclusions.

Details of the cross section of the ZBH disc are shown in Figure 13. The oxide layer did not spall off or fracture, confirming good adhesion to the un-oxidized bulk, Figure 13a. Then in Figure 13b the oxidation products of the initial $(\text{Zr},\text{Hf})\text{B}_2$ solid solution composed of ZrO_2 grains encasing HfO_2 nano-inclusions may be observed. Figure 13c&d shows the carbon fiber-depleted site partially filled with HfSi_2 or HfC oxidation products, silica and HfO_2 , according to reaction (6).



Images of the cross section of the ZBW disc are shown in Figure 14. The oxide layer spalled off after torch testing, probably due to both the high temperature achieved, 2240°C , and the initial lack of densification, Figure 14a. In the residual outer oxide layer, C fibers were completely removed leaving ZrO_2 grains with an intergranular WO_3 phase, Figure 14c&d. A closer view of the ZrO_2 grains, however, rarely showed the formation of W-nano inclusions previously observed upon oxidation of a similar $(\text{Zr},\text{W})\text{B}_2$ solid solution [27] and in contrast to the previous two materials. This is possibly due to the local chemical environment being rich in CO/CO_2 from the fiber oxidation, rather than B_2O_3 arising from the boride oxidation reaction (equation 3). As the temperature profile decreased from the hottest location, silica was found filling the fiber cavities with round crystalline precipitates containing W and Zr, Figure 14e&f. Further inside, close to the boride/oxide interface, the carbon fibers were still present but generally covered by silica-based glass and W-oxides, identifiable by the bright contrast.

3.4 Ablation resistance of the composites

The great benefit of the introduction of a large volume fraction of fiber is clearly demonstrated in this study, since all materials withstood the high-enthalpy torch test and the high thermal shock associated with it and none of them shattered into pieces despite the high initial heating rate. In addition, none of the materials led to the formation of columnar zirconia in the oxide sub-scales, which is very detrimental to the protection of the composite. This is probably due to the effect of scattered discontinuous fibers that hindered a straightforward gases leak and growth

of zirconia in vertical columnar pillars. Similar outcomes were observed when SiC short fiber were added to ZrB₂ [32]. However, different responses to the oxyacetylene flame were observed in this work depending on the nature of the secondary phase introduced, Figure 4. After these first torch tests it seems that all the materials considered displayed similar behavior in terms of their oxidation mechanisms, weight variation and microstructural features. However, if there is interest in using them as reusable materials, some compositions will have more chance of success in terms of durability. Therefore it is important to understand the causes of this different behavior between one composition and the next. It is apparent that the replacement of 5 vol% of SiC with a silicide is not always a benefit for the ablation behavior.

If we first consider the weight change behavior, we have to assess that it is not the most reliable measure of oxidation resistance for such materials with different constituents forming different volatile products (e.g. MoO₃, WO₃ or SiO) and can complicate the interpretation of the results. However, comparison of the relative weight changes for the simple oxidation reactions of the MeSi₂ vs SiC additions could provide baseline information. Therefore, Table 4 collects the main oxidation reactions for SiC and silicides and the relative weight change per mole of O₂. Under the hypothesis that silica is pure (without cation doping) and is not splashed away by the torch flux, similar weight gain occurs for SiC and HfSi₂, whilst weight loss occurs for MoSi₂ and WSi₂ additions. This calculation only partially reflects the observed behavior (HfSi₂ doping is the best), confirming that cation-doped silica glass is more beneficial for the oxidation behavior as compared to pure silica glass.

Effect of residual porosity - The first effect of the addition of the different silicides arose from the initial densification. The different degrees of densification achieved, 92% for ZBM, 94% for ZBH and 84% for ZBW, can be related to the melting points of the transient liquid phases formed during sintering that favored the mass transfer mechanism in a more or less effective manner [25]. Establishing the exact composition of the melts and the temperature at which these formed is out of the scope of this paper, since the large abundance of C, derived from the high

volume content of fiber and the hot press components, plus the oxides present as impurities in the starting powders, make calculations too difficult. However, if the pure Me-Si systems are considered [34], liquid phases appear at the lowest temperature in the Hf-Si system, \sim 1325°C, followed by Mo-Si, \sim 1900°C, and W-Si, \sim 2000°C, in agreement with the final density achieved. This speculation can partially justify the observed density variation of the matrices in the materials containing MeSi₂. As for the baseline material, the thin silica coating covering the SiC particles will have efficiently promoted densification. The fact that none reached full density is certainly due to the consumption of the liquid phases by the carbon fiber through reaction to form solid products, such as SiC and Me-C compounds [7].

Temperatures ranging from 2076 to 2241°C were achieved on the surface, Figure 3. Given these variations of actual temperatures experienced by the materials, it is difficult to establish a performance ranking. However based on the similar density criterion, we can reasonably compare the baseline ZBS with ZBM and ZBH, which possess relative densities between 92 and 94% of the theoretical density.

Concerning the effect of the introduction of a transition metal silicide on the ablation resistance of these ZrB₂-SiC-Cf UHTCMCs, we cannot draw a universal conclusion. Figure 4 clearly displays that some additives outperform SiC, such as HfSi₂ which has the thinnest oxide scale and lowest weight loss, whilst others are detrimental, such as MoSi₂ and WSi₂. The cross section analysis of Figure 10 further shows that although ZBS experienced the lowest peak temperature, 2076°C, the oxide scale was more than twice as thick as that on the ZBH, which reached 2105°C, though only 40 µm of scale resulted.

Oxide thickness and stability - The oxide thickness in ZBS was more comparable to the ZBM which achieved 2168°C, i.e. 100°C higher than the reference baseline material. In this perspective, modification of the chemistry of the baseline with Hf compounds are suggested for improving the ablative properties of such fiber-rich composites. The scientific reason is understandable looking at the phase stability diagram shown in Figure 15.

The effect of MoSi₂ and HfSi₂, which attained similar density levels, 92-94%, and achieved close surface temperatures, 2105-2170°C, can be approximated. From SEM investigation of the cross section, the oxide scale is remarkably different in the two materials, 125 and 40 µm, respectively. It can be speculated that, beside an approximate 70°C temperature effect, the oxidation behavior of the two additives influences the overall response of the materials.

The oxidation of these systems is mainly defined by oxygen inward diffusion through the sample and the outward diffusion of, mainly, B₂O₃ and CO/CO₂ towards the sample surface, as a consequence of the oxidation of the ZrB₂ matrix and C fibers, respectively, and of lower amounts of SiO/SiO₂ due to SiC oxidation.

If the Zr-B-O system is considered, the introduction of MoSi₂ to a boride matrix yielded MoB and MoO₃ as oxidation products, see the blue line in Figure 15a. At high oxygen partial pressures and low B₂O₃ partial pressure, that is in the outer oxide scales, the most favorable products will have been Mo-oxides, which are highly volatile [30]. A similar behavior was found for WSi₂ additions to the boride matrix, with the formation of volatile W-oxides [31]. In contrast, according to the predominance diagrams, HfSi₂ could yield HfB₂ and HfO₂ which remained solid up to 2760°C, see the red lines in Figure 15a. The presence of volatile compounds, such as Mo-oxides or W-oxides, both within the ZrO₂ grains and at the triple junctions, results in pores and voids throughout the oxide scale, which all contribute to the embrittlement of the scale. On the other hand, solid HfO₂ guarantees a higher oxide density and thus less channels are available for oxygen penetration through the bulk.

The presence of large amounts of carbon fibers complicates the system, but does not change the overall picture. In proximity to the fiber sites, the material is locally saturated in CO instead of B₂O₃, Figure 15b. For MoSi₂ addition, the Me-C-O predominance diagram indicates formation of various species including Mo-oxides and carbides, which are unstable. Similar considerations hold for WC additions. It follows that the development of bubbles and zirconia embrittlement will be even faster in ZBM (and ZBW) as a result of rapid vaporization at high temperatures. In contrast,

for HfSi₂ additions in ZBH, the higher stability of HfC, Hf-C-O and HfO₂ as solid products will yield a higher density zirconia-scale, even compared to the ZBS.

So, to answer the initial question about the effect of MeSi₂ on the ablation behavior of this new class of composites, the experiments performed demonstrated that not all MeSi₂ are to be preferred to SiC additions. Actually, for MoSi₂, HfSi₂ and WSi₂, only the material containing HfSi₂ proved superior to the baseline material owing to its increased capability to promote the elimination of porosity during densification and to the refractory nature of its corresponding oxide, HfO₂, which remains a solid compound up to 2760°C. In contrast, MoSi₂ and WSi₂, although form oxidation products which are stable in the sub-scales, form highly volatile oxides on the surface which do not offer better protection than a pure ZrO₂ scale developed in the presence of just SiC.

4. Conclusions

The aero-thermal behavior of ZrB₂ ceramics containing 40 vol% of chopped carbon fiber, 5 vol% SiC and 5 vol% of various transition metal silicides, MoSi₂, HfSi₂ and WSi₂, has been evaluated using an oxyacetylene torch at T>2000°C and compared to a baseline composite containing only 10 vol% of SiC. All composites successfully resisted the harsh conditions and none of them shattered, nor developed columnar ZrO₂-grains in the outer-scale, which is generally considered the precursor step before catastrophic material oxidation. Different front and back temperatures were achieved mainly depending on the material porosity and hence its thermal conductivity. The thickness of the growing oxide layer may have also played a role.

The material containing HfSi₂ (ZBH) showed the highest capability to resist oxidation in these demanding conditions due to the formation of an adherent oxide scale with a thickness of just 40 µm, thanks to the local formation of solid HfC or HfO₂. The other two silicides allowed the oxidation of a thicker portion of material, around 122-125 µm, owing to the formation of volatile Mo- and W-oxides which embrittled the zirconia outer structure. The higher front and back

temperature of ZBW compared to ZBM, despite the similar oxide scale thickness, was attributed to the higher initial porosity of the former (17%) compared to that of ZBM (9%).

In view of these results, these new materials are believed to show promise and potential for use in ultra-high temperature applications such as thermal protection systems and solid/hybrid-propellant rocket nozzles.

Acknowledgements

This work has received funding from the European Union's Horizon 2020 "Research and innovation programme" under grant agreement No. 685594 (C³HARME). C. Melandri is acknowledged for roughness measurements and strength tests.

Data availability

The raw and processed data required to reproduce these findings cannot be shared at this time due to legal or ethical reasons.

References

- [1] D. Sciti, R. Savino, L. Silvestroni, Aerothermal behaviour of a SiC fibre-reinforced ZrB₂ sharp component in supersonic regime, *J. Eur. Ceram. Soc.* 32 (2012) 1837–1845. doi:10.1016/j.jeurceramsoc.2012.01.019.
- [2] L. Silvestroni, D. Sciti, G.E. Hilmas, W.G. Fahrenholtz, J. Watts, Effect of a weak fiber interface coating in ZrB₂ reinforced with long SiC fibers, *Mater. Des.* 88 (2015) 610–618. doi:10.1016/j.matdes.2015.08.105.
- [3] L. Silvestroni, E. Landi, K. Bejtka, A. Chiodoni, D. Sciti, Oxidation behavior and kinetics of ZrB₂ containing SiC chopped fibers, *J. Eur. Ceram. Soc.* 35 (2015) 4377–4387. doi:10.1016/j.jeurceramsoc.2015.07.024.
- [4] D. Sciti, L. Silvestroni, G. Saccone, D. Alfano, Effect of different sintering aids on thermo-mechanical properties and oxidation of SiC fibers - Reinforced ZrB₂ composites, *Mater. Chem. Phys.* 137 (2013) 834–842. doi:10.1016/j.matchemphys.2012.09.071.
- [5] L. Silvestroni, D.D. Fabbriche, D. Sciti, Tyranno SA3 fiber-ZrB₂ composites. Part I: Microstructure and densification, *Mater. Des.* 65 (2015) 1253–1263.

- doi:<http://dx.doi.org/10.1016/j.matdes.2014.08.068>.
- [6] L. Zoli, V. Medri, C. Melandri, D. Sciti, Continuous SiC fibers-ZrB₂ composites, *J. Eur. Ceram. Soc.* 35 (2015) 4371–4376. doi:[10.1016/j.jeurceramsoc.2015.08.008](https://doi.org/10.1016/j.jeurceramsoc.2015.08.008).
 - [7] L. Silvestroni, D. Dalle Fabbriche, C. Melandri, D. Sciti, Relationships between carbon fiber type and interfacial domain in ZrB₂-based ceramics, *J. Eur. Ceram. Soc.* 36 (2016) 17–24. doi:[10.1016/j.jeurceramsoc.2015.09.026](https://doi.org/10.1016/j.jeurceramsoc.2015.09.026).
 - [8] D. Sciti, L. Zoli, L. Silvestroni, A. Cecere, G.D. Di Martino, R. Savino, Design, fabrication and high velocity oxy-fuel torch tests of a Cf-ZrB₂- fiber nozzle to evaluate its potential in rocket motors, *Mater. Des.* 109 (2016) 709–717. doi:[10.1016/j.matdes.2016.07.090](https://doi.org/10.1016/j.matdes.2016.07.090).
 - [9] A. Vinci, L. Zoli, E. Landi, D. Sciti, Oxidation behaviour of a continuous carbon fibre reinforced ZrB₂-SiC composite, *Corros. Sci.* 123 (2017) 129-138. doi:[10.1016/j.corsci.2017.04.012](https://doi.org/10.1016/j.corsci.2017.04.012)
 - [10] L. Silvestroni, C. Capiani, D.D. Fabbriche, C. Melandri, Novel light and tough ZrB₂-based functionally graded ceramics, *Compos. Part B Eng.* 99 (2016) 321–329. doi:<https://doi.org/10.1016/j.compositesb.2016.06.001>.
 - [11] J.J. Sha, J. Li, S.H. Wang, Z.F. Zhang, Y.F. Zu, S. Flauder, W. Krenkel, Improved microstructure and fracture properties of short carbon fiber-toughened ZrB₂-based UHTC composites via colloidal process, *Int. J. Refract. Met. Hard Mater.* 60 (2016) 68–74. doi:[10.1016/j.ijrmhm.2016.07.010](https://doi.org/10.1016/j.ijrmhm.2016.07.010).
 - [12] F. Yang, X. Zhang, J. Han, S. Du, Processing and mechanical properties of short carbon fibers toughened zirconium diboride-based ceramics, *Mater. Des.* 29 (2008) 1817–1820. doi:[10.1016/j.matdes.2008.03.011](https://doi.org/10.1016/j.matdes.2008.03.011).
 - [13] L. Li, Y. Wang, L. Cheng, L. Zhang, Preparation and properties of 2D C/SiC–ZrB₂–TaC composites, *Ceram. Int.* 37 (2011) 891–896. doi:<https://doi.org/10.1016/j.ceramint.2010.10.033>.
 - [14] S. Tang, J. Deng, S. Wang, W. Liu, K. Yang, Ablation behaviors of ultra-high temperature ceramic composites, *Mater. Sci. Eng. A.* 465 (2007) 1–7. doi:[10.1016/j.msea.2007.02.040](https://doi.org/10.1016/j.msea.2007.02.040).
 - [15] H. Hu, Q. Wang, Z. Chen, C. Zhang, Y. Zhang, J. Wang, Preparation and characterization of C/SiC–ZrB₂ composites by precursor infiltration and pyrolysis process, *Ceram. Int.* 36 (2010) 1011–1016. doi:<https://doi.org/10.1016/j.ceramint.2009.11.015>.
 - [16] Q. Li, S. Dong, Z. Wang, G. Shi, Fabrication and properties of 3-D Cf/ZrB₂-ZrC-SiC composites via polymer infiltration and pyrolysis, *Ceram. Int.* 39 (2013) 5937–5941. doi:[10.1016/j.ceramint.2012.11.074](https://doi.org/10.1016/j.ceramint.2012.11.074).
 - [17] A. Paul, S. Venugopal, J.G.P. Binner, B. Vaidhyanathan, A.C.J. Heaton, P.M. Brown,

- UHTC-carbon fibre composites: Preparation, oxyacetylene torch testing and characterisation, *J. Eur. Ceram. Soc.* 33 (2013) 423–432. doi:10.1016/j.jeurceramsoc.2012.08.018.
- [18] L.G. L. Liu, H. Li, W. Feng, X. Shi, K. Li, Ablation in different heat fluxes of C/C composites modified by ZrB₂-ZrC and ZrB₂-ZrC-SiC particles, *Corros. Sci.* 74 (2013) 159–167. doi:doi:10.1016/j.corsci.2013.04.038.
- [19] X.S. C. Tian, D. Gao, Y. Zhang, C. Xu, Y. Song, Oxidation behaviour of zirconium diboride-silicon carbide ceramic composites under low oxygen partial pressure, *Corros. Sci.* 53 (2011) 3742–3746. doi:doi:10.1016/j.corsci.2011.07.020.
- [20] E.J. Wuchina, E. Opila, M. Opeka, W.G. Fahrenholtz, I. Talmy, UHTCs: Ultra-high temperature ceramic materials for extreme environment applications, *Electrochem. Soc. Interfaces*. 16 (2007) 30–36.
- [21] S.N. Karlsdottir, J.W. Halloran, Oxidation of ZrB₂-SiC: Influence of SiC content on solid and liquid oxide phase formation, *J. Am. Ceram. Soc.* 92 (2009) 481–486. doi:10.1111/j.1551-2916.2008.02874.x.
- [22] L. Silvestroni, D. Sciti, Oxidation of ZrB₂ ceramics containing SiC as particles, whiskers, or short fibers, *J. Am. Ceram. Soc.* 94 (2011) 2796–2799. doi:10.1111/j.1551-2916.2011.04726.x.
- [23] M. Kazemzadeh Dehdashti, W.G. Fahrenholtz, G.E. Hilmas, Effects of transition metals on the oxidation behavior of ZrB₂ ceramics, *Corros. Sci.* 91 (2015). doi:doi:10.1016/j.corsci.2014.11.019.
- [24] L. Silvestroni, G. Meriggi, D. Sciti, Oxidation behavior of ZrB₂ composites doped with various transition metal silicides, *Corros. Sci.* 83 (2014) 281–291.
- [25] D. Sciti, L. Silvestroni, V. Medri, F. Monteverde, Sintering and Densification Mechanisms of Ultra-High Temperature Ceramics, 2014. doi:10.1002/9781118700853.ch6.
doi:10.1016/j.corsci.2014.02.026.
- [26] L. Silvestroni, S. Failla, I. Neshpor, O. Grigoriev, Method to improve the oxidation resistance of ZrB₂-based ceramics for reusable space systems, *J. Eur. Ceram. Soc.* 38 (2018) 2467–2476. doi:10.1016/j.jeurceramsoc.2018.01.025.
- [27] L. Silvestroni, D. Sciti, F. Monteverde, K. Stricker, H.-J. Kleebe, Microstructure evolution of a W-doped ZrB₂ ceramic upon high-temperature oxidation, *J. Am. Ceram. Soc.* 100 (2017). doi:10.1111/jace.14738.
- [28] L. Silvestroni, K. Stricker, D. Sciti, H.-J. Kleebe, Understanding the oxidation behavior of a ZrB₂–MoSi₂ composite at ultra-high temperatures, *Acta Mater.* 151 (2018). doi:10.1016/j.actamat.2018.03.042.

- [29] L. Silvestroni, M. Nygren, D. Sciti, Study of the interactions between HfB₂ and Hi-Nicalon™ fiber, *J. Eur. Ceram. Soc.* 33 (2013). doi:10.1016/j.jeurceramsoc.2013.07.004.
- [30] E.A. Gulbransen, K.F. Andrew, F.A. Brassart, Oxidation of Molybdenum 550° to 1700°C, *J. Electrochem. Soc.* 110 (1963) 952. doi:10.1149/1.2425918.
- [31] E.A. Gulbransen, K.F. Andrew, F.A. Brassart, Kinetics of Oxidation of Pure Tungsten, 1150°–1615°C, *J. Electrochem. Soc.* 111 (1964) 103–109. doi:10.1149/1.2426043.
- [33] D. Sciti, R. Savino, L. Silvestroni, Aerothermal behaviour of a SiC fibre-reinforced ZrB₂ sharp component in supersonic regime, *J. Eur. Ceram. Soc.* 32 (2012). doi:10.1016/j.jeurceramsoc.2012.01.019.
- [34] C. Vahlas, P.Y. Chevalier, E. Blanquet, A thermodynamic evaluation of four Si-M (M = Mo, Ta, Ti, W) binary systems, *Calphad.* 13 (1989) 273–292. doi:10.1016/0364-5916(89)90007-2.

Tables

Powder	Grade and Supplier	d_{50} / μm	Purity / wt%	Main impurities / wt%
ZrB ₂	B, H.C. Starck, Germany	2.3	>98	O:0.8, Hf:1.82, N:0.19
SiC	UF-25, H.C. Starck, Germany	0.42	>99	O:1.7, Fe:0.04, Al:0.03
MoSi ₂	<2 micron, Aldrich, Germany	2.94	>99	O:1.0
HfSi ₂	in-house synthesized [36]	3.5	-	O:0.1, C:0.07
WSi ₂	-325 mesh, Sigma Aldrich, Italy	-	>99.5	metal traces <6000 ppm
Cf	XN-60C-03S, Nippon Graphite Fiber, Japan	\varnothing : 10 length 3000	-	size content: 2.9 epoxy resin

Table 1: Main characteristics of the raw powders and fiber used.

Sample	Additive / vol%	Rel. ρ / %	Porosity / %	Specific weight loss / % cm^{-2}	Oxide layer thickness / μm	σ_{RT} / MPa	σ_{1500} / MPa
ZBS	10 SiC	92.8	7	0.007	95+2	135±3	n.a.
ZBM	5 SiC, 5 MoSi ₂	91.5	9	0.012	125+6	116±1	201±2
ZBH	5 SiC, 5 HfSi ₂	93.7	6	0.004	40+3	137±7	n.a.
ZBW	5 SiC, 5 WSi ₂	83.5	17	0.015	>122+6*	102±1	143±1

*oxide spall-off during the torch test

Table 2: Composition, relative density (ρ) and residual porosity of the ZrB₂ materials containing 40 vol% of chopped Cf hot pressed at 1900°C for 30 min under 40 MPa, specific weight loss upon the test, thickness of the oxide scale formed in the hottest zone and 4-point strength at room temperature and 1500°C in Ar.

Sample	As-machined surfaces			Surface upon torch test		
	R _{a0} / μm	S _{a0} / μm	S _{q0} / μm	R _a / μm	S _a / μm	S _q / μm
ZBS	0.69±0.15	1.3	2.0	1.42±0.12	8.6	16.2
ZBM	0.43±0.12	1.2	2.1	1.30±0.14	18.6	26.7
ZBH	0.35±0.06	1.2	1.7	3.02±0.32	11.4	15.1
ZBW	0.40±0.06	1.4	1.9	1.18±0.16	19.3	27.6

Table 3: Roughness parameters before and after torch test. Ra: mean linear roughness, Sa: mean surface roughness, Sq: root mean squared height.

SH phase	Reaction	Δwt%
SiC	SiC + 1.5O _{2(g)} → SiO _{2(l)} + CO _(g)	50.0
MoSi ₂	MoSi ₂ + 3.5O _{2(g)} → 2SiO _{2(l)} + MoO _{3(g)}	-21.0
HfSi ₂	2HfSi ₂ + 6O _{2(g)} → 4SiO _{2(l)} + 2HfO ₂	40.9
WSi ₂	WSi ₂ + 3.5O _{2(g)} → 2SiO _{2(l)} + WO _{3(g)}	-49.9

Table 4: Relative weight change per mole of O₂ for the basic oxidation reactions of the various self-healing (SH) phases.

Figures captions

Figure 1: Schematics of the oxy-acetylene torch experimental arrangement.

Figure 2: SEM micrographs of the short Cf composites showing a) an overview of the baseline composite microstructure containing 10 vol% SiC and, at higher magnification, samples containing 5 vol% SiC particles and 5 vol% of b) MoSi₂, c) HfSi₂ and d) WSi₂. The inset in c) is an enlarged view of the fiber/matrix interface showing the formation of HfC nano-crystals.

Figure 3: a) Plot of the maximum temperature achieved on the front and back surfaces measured by 2-color pyrometer and thermal infra-red camera during OAT testing and b) the temperature profiles measured by 2-CP on the front surfaces for all the UHTCMCs.

Figure 4: Images of the discs before, during and after torch testing.

Figure 5: 2D (left) and 3D (right) topographic maps of the torched discs.

Figure 6: (a-c) SEM images taken in the most damaged region of the outer surface of the baseline disc upon torch tests, overview (a) and microstructure details (b, c). (d-e) Microstructure outlook in the outskirt of the disc evidencing the presence of SiO₂-glass at the fiber sites and nanosized ZrO₂ grains.

Figure 7: (a-c) SEM images taken in the most damaged region of the outer surface of the ZBM disc after torch testing, overview (a) and microstructural details (b&c). The inset in a) shows exfoliation of the surface. (d&e) Microstructure outlook at the edge of the disc showing the presence of SiO₂-glass in the fiber sites with the corresponding EDS spectrum.

Figure 8: (a-c) SEM images taken in the most damaged region of the outer surface of the ZBH disc after torch testing, overview (a) and microstructural details (b&c). The inset in a) shows the EDS spectra of ZrO₂ and HfO₂. (d&e) Microstructure outlook at the edge of the disc showing the presence of SiO₂-glass in the fiber sites with the corresponding EDS spectrum.

Figure 9: (a-c) SEM images taken in the most damaged region of the outer surface of the ZBW disc after torch testing, overview (a) and microstructural details (b&c). The inset in a) shows the EDS

spectra of ZrO₂ with W-based inclusions. (d-f) Microstructure outlook at the edge of the disc showing the presence of SiO₂-glass in the fiber sites with the corresponding EDS spectrum.

Figure 10: SEM images of the most damaged areas of the disc cross sections showing the respective oxide thicknesses.

Figure 11: SEM images of the cross section of the baseline disc showing microstructural details after torch testing.

Figure 12: SEM images of the cross section of the ZBM disc showing microstructural details after torch testing and below the EDS spectra of MoSi₂ oxidation products.

Figure 13: SEM images of the cross section of the ZBH disc showing microstructural details after torch testing with the EDS spectra of the oxidation products.

Figure 14: SEM images of the cross section of the ZBW disc showing microstructural details upon torch testing with the EDS spectra of the oxidation products.

Figure 15: Phase stability diagrams for the Zr- (black), Hf- (red) and Mo- (blue) systems calculated at 2000°C as a function of oxygen and a) boron oxide partial pressures or b) carbon oxide partial pressures.

Fig. 1

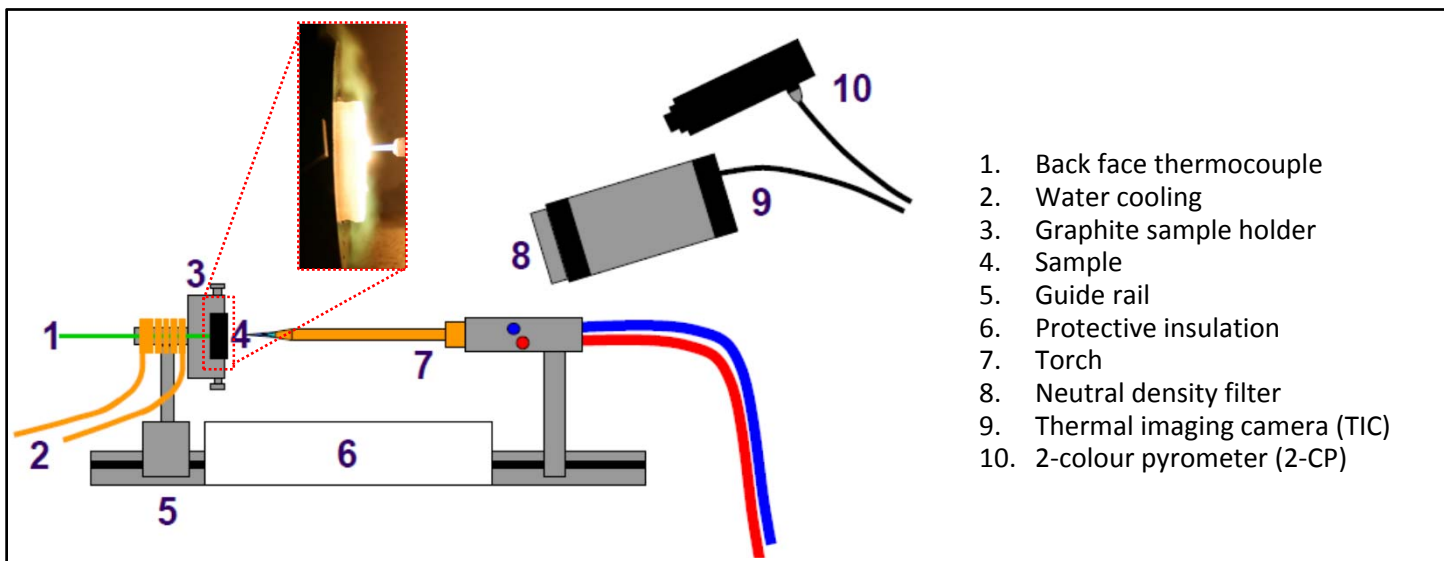


Fig. 2

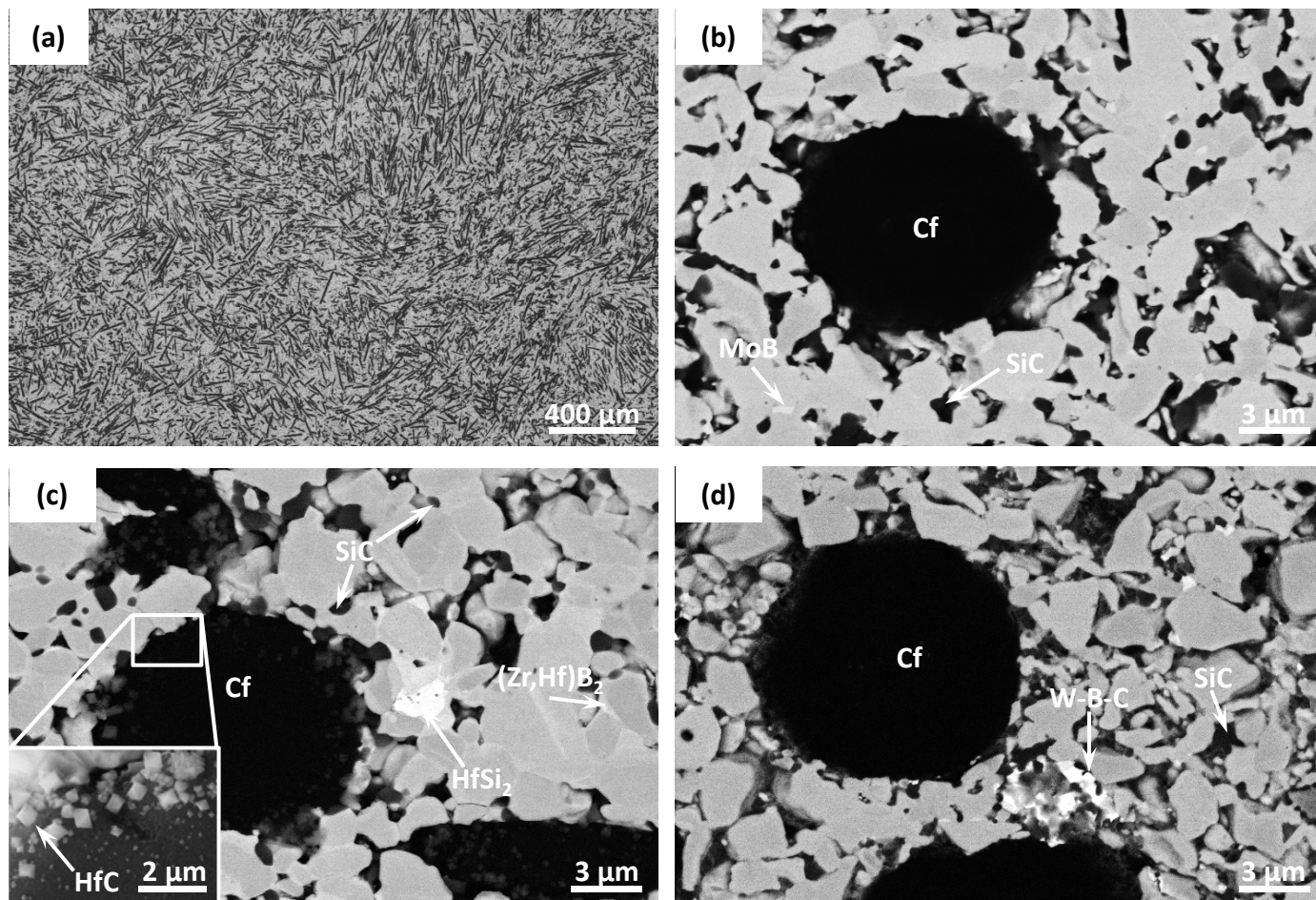


Fig. 3

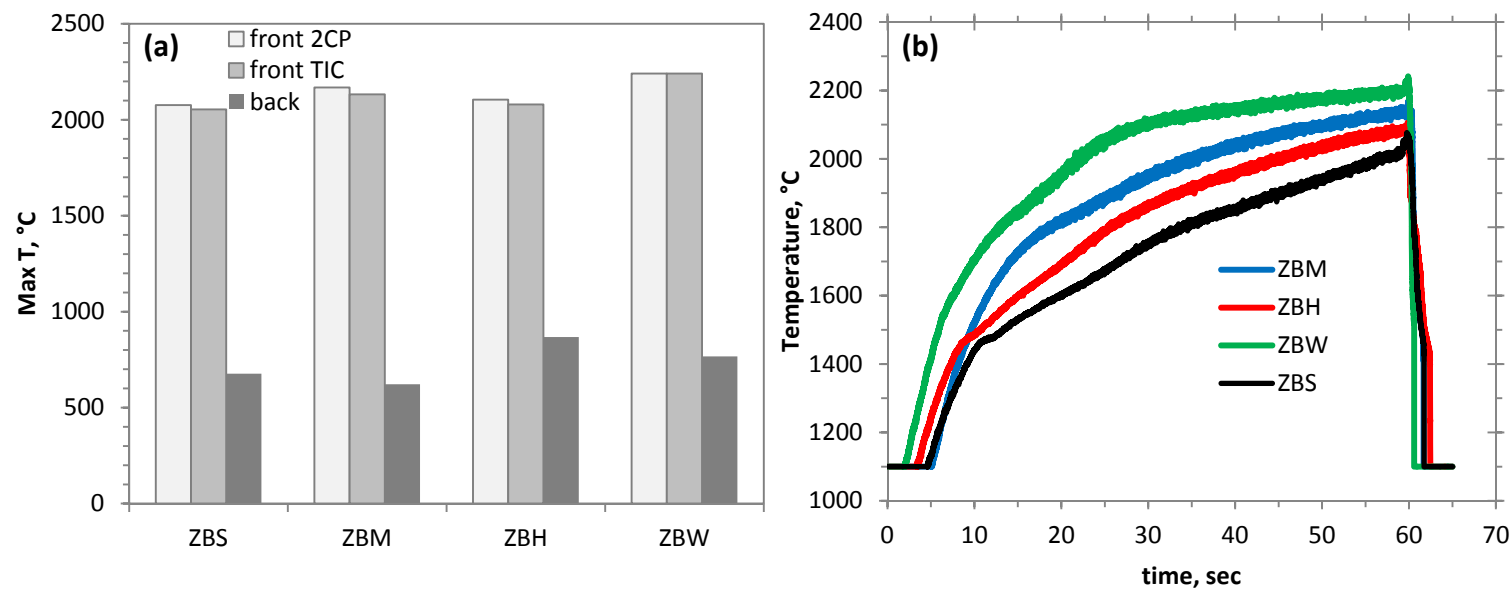


Fig. 4

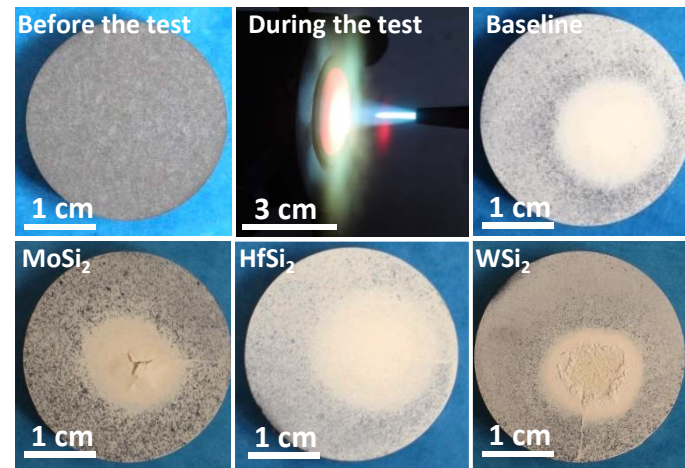


Fig. 5

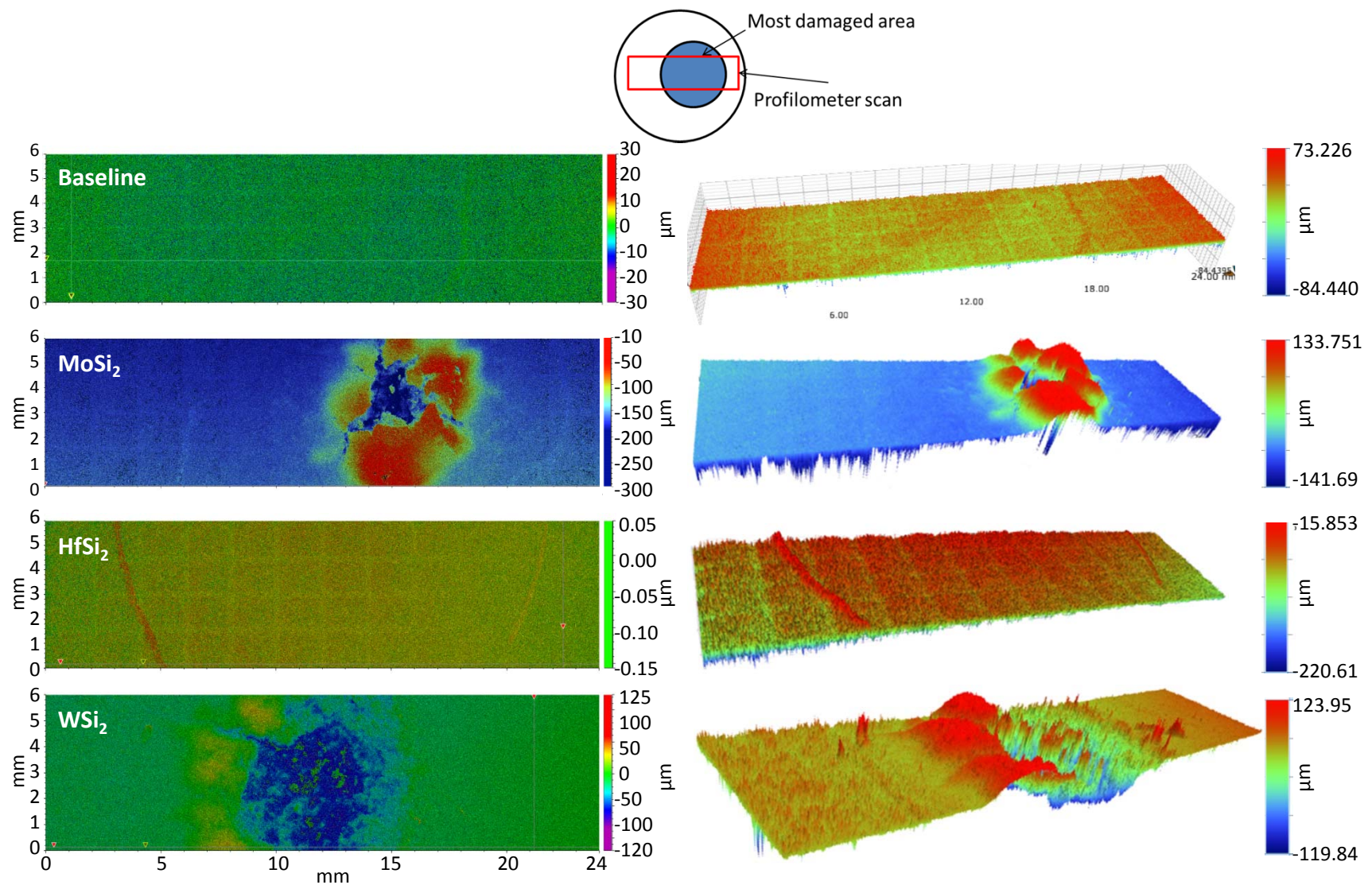


Fig. 6

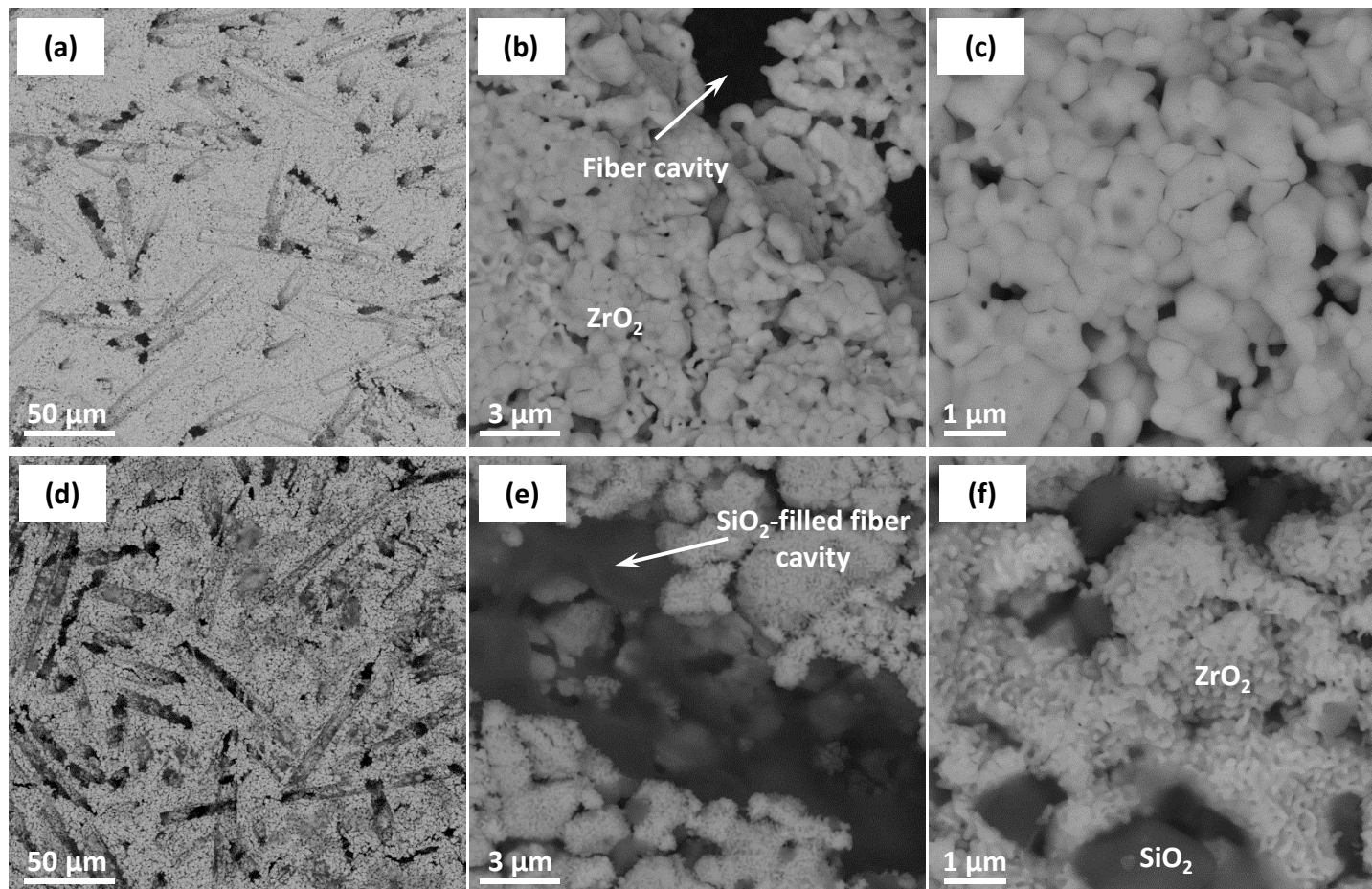


Fig. 7

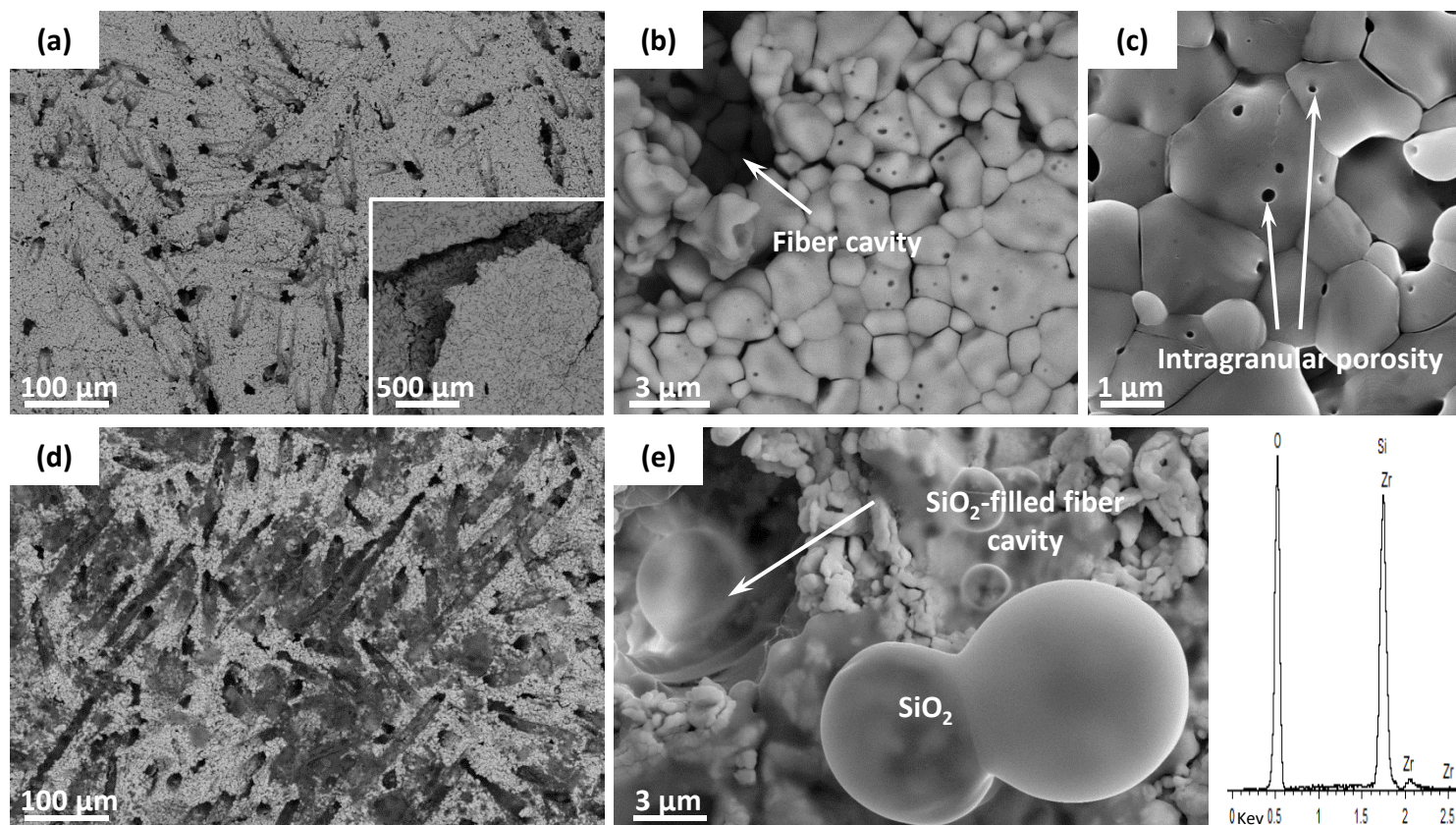


Fig. 8

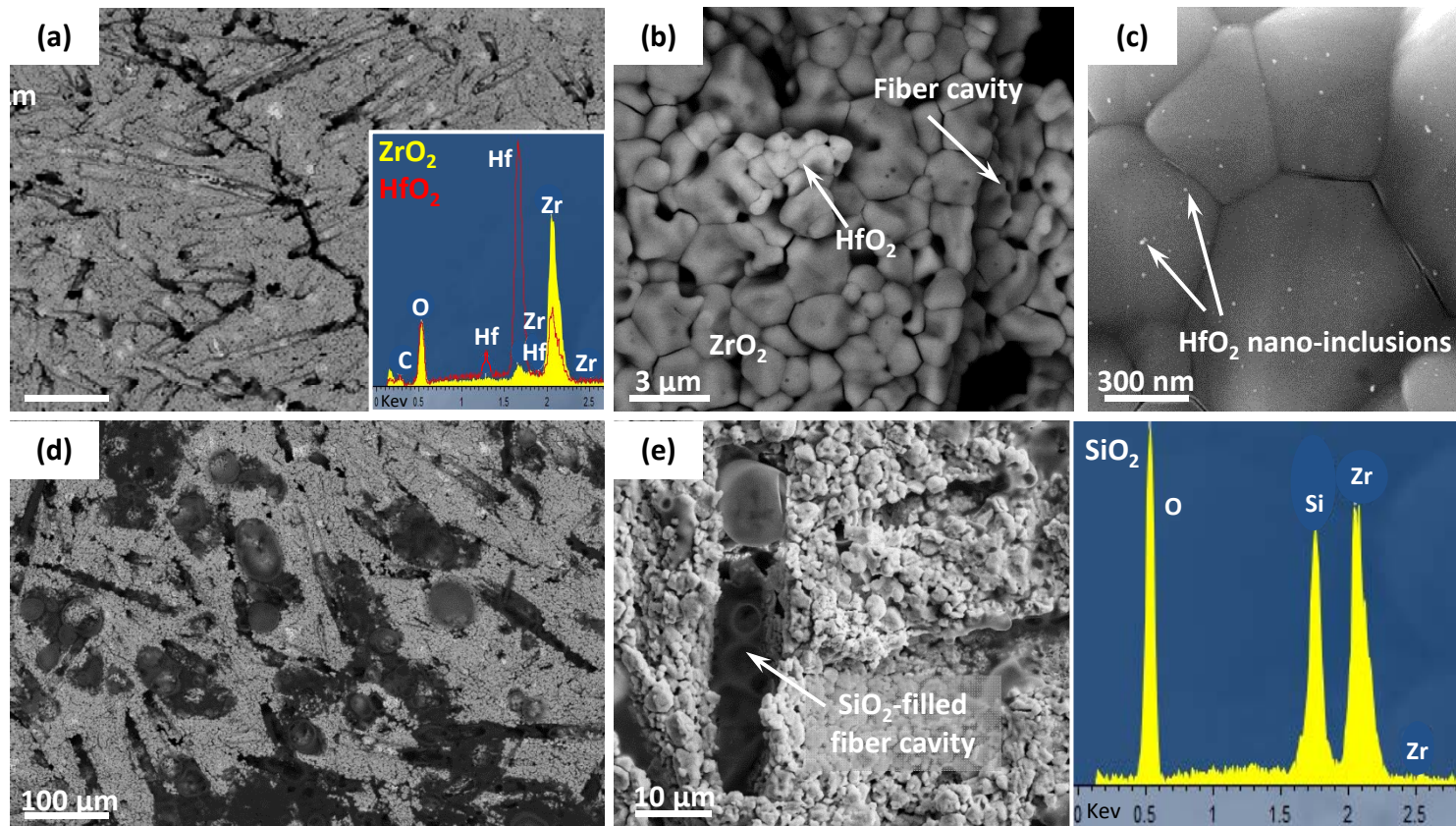


Fig. 9

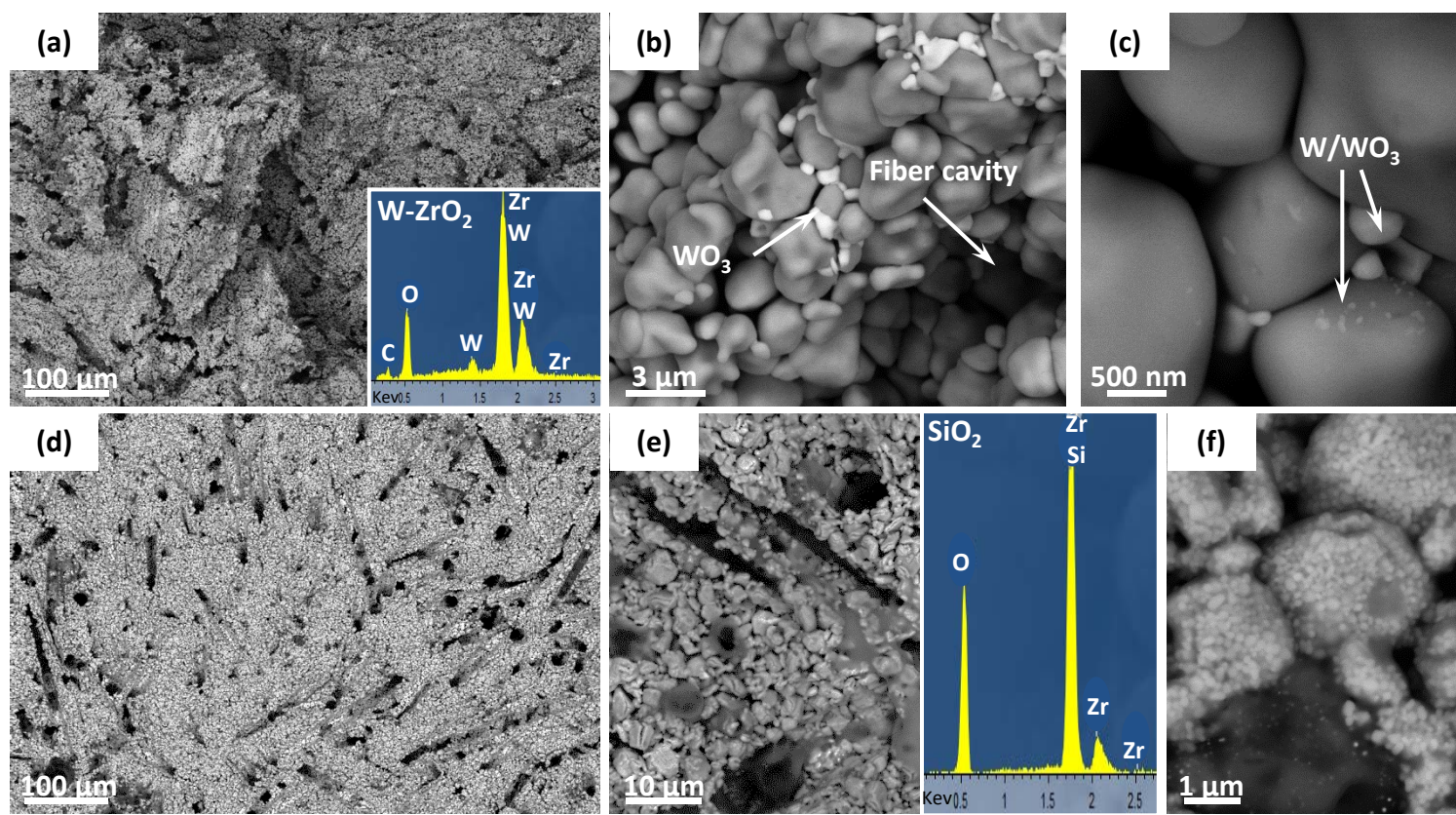


Fig. 10

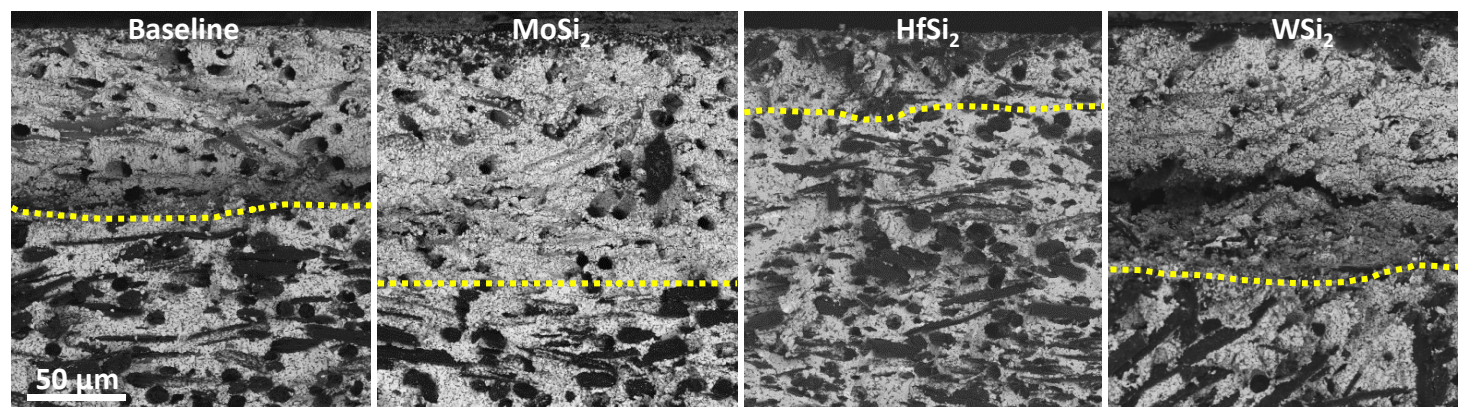


Fig. 11

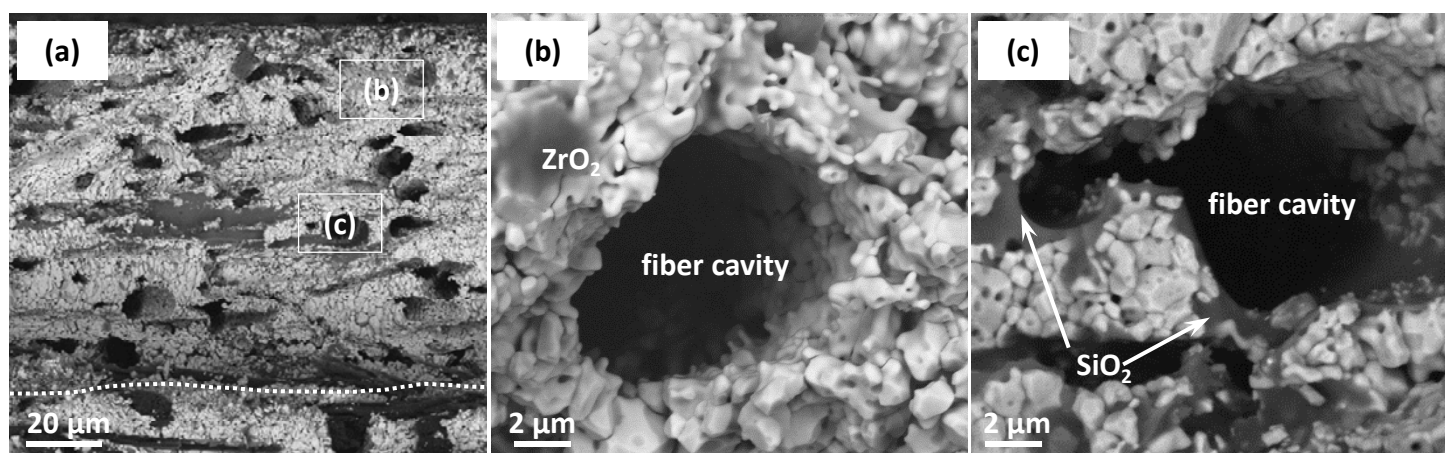


Fig. 12

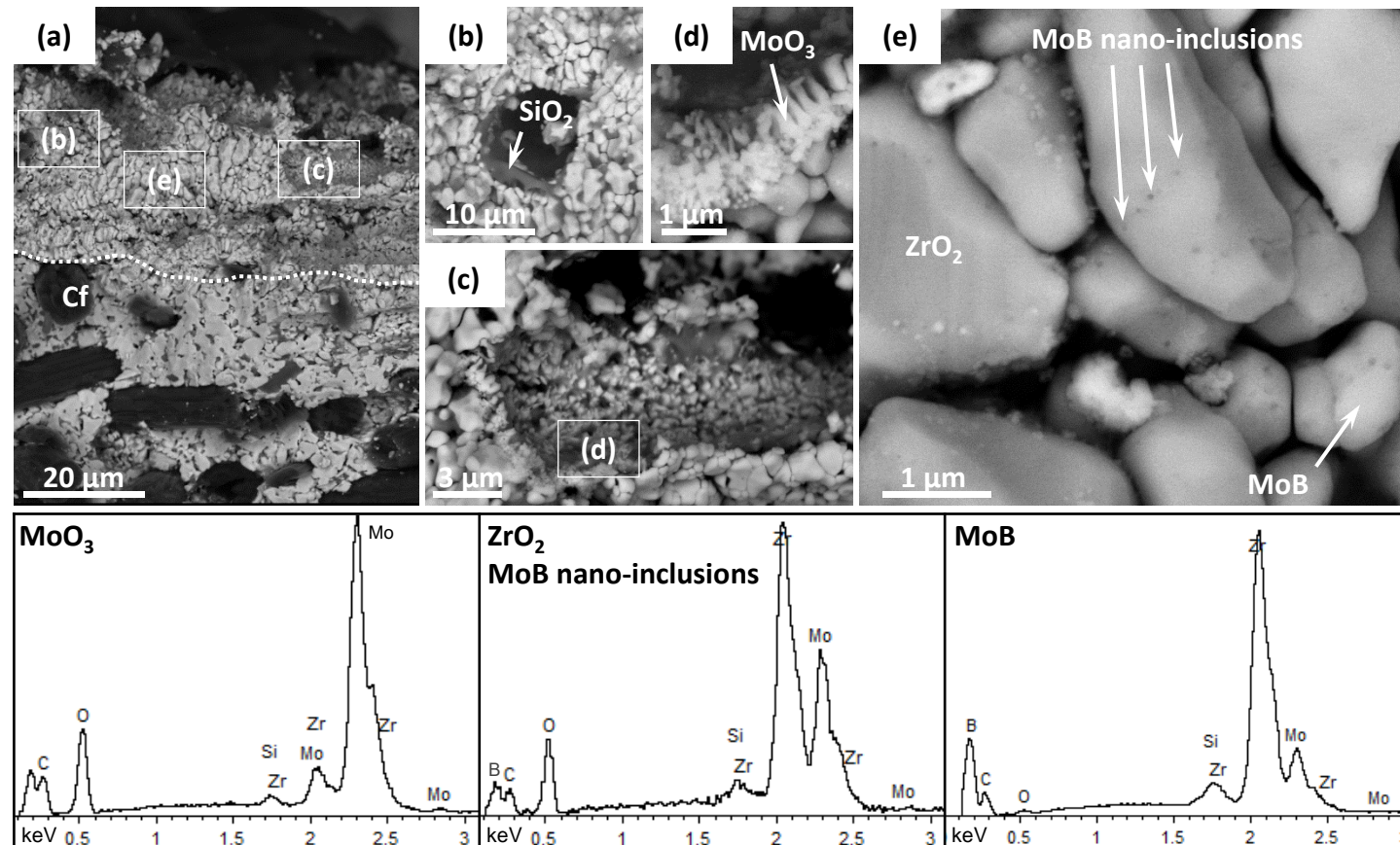


Fig. 13

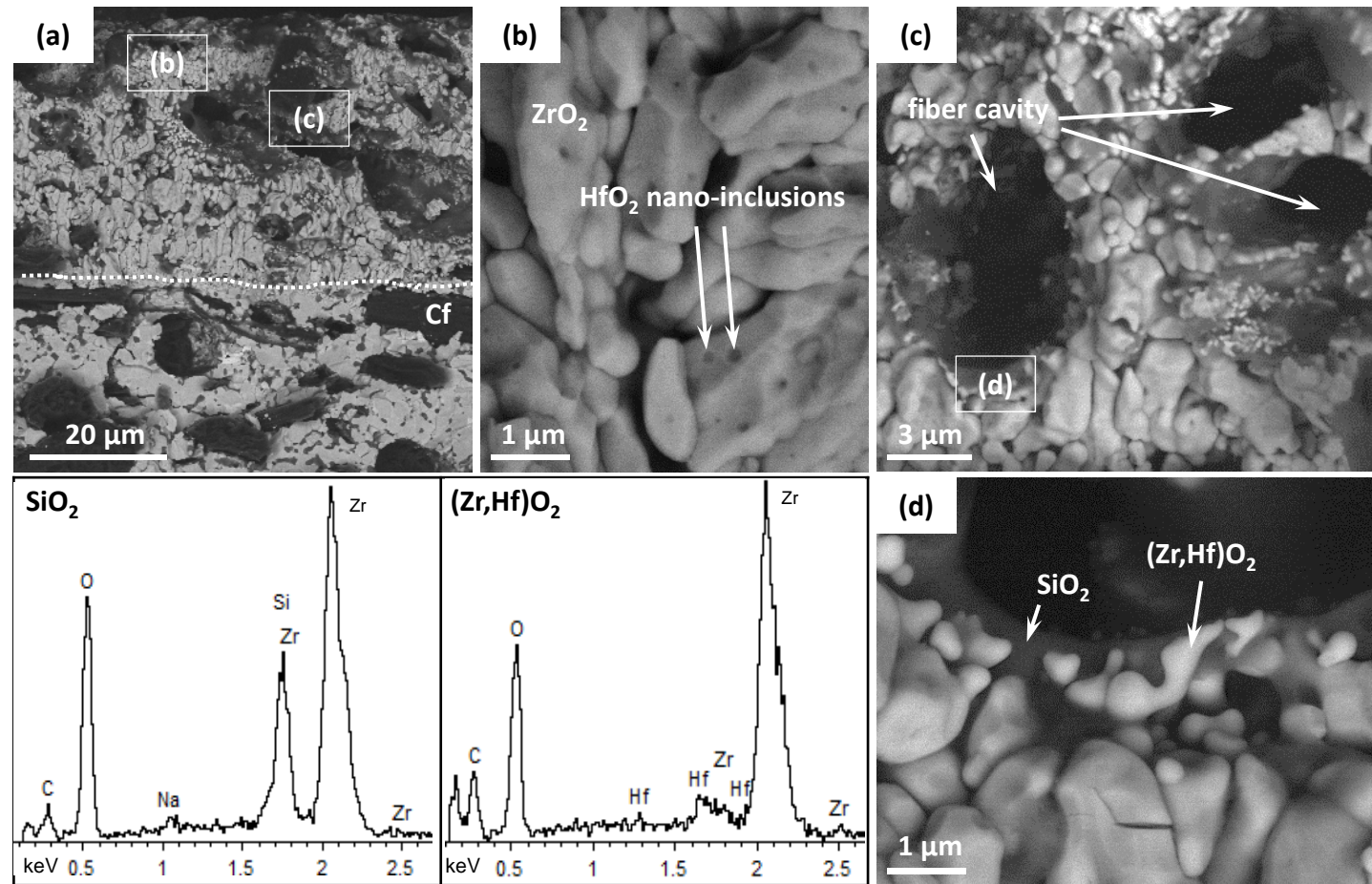


Fig. 14

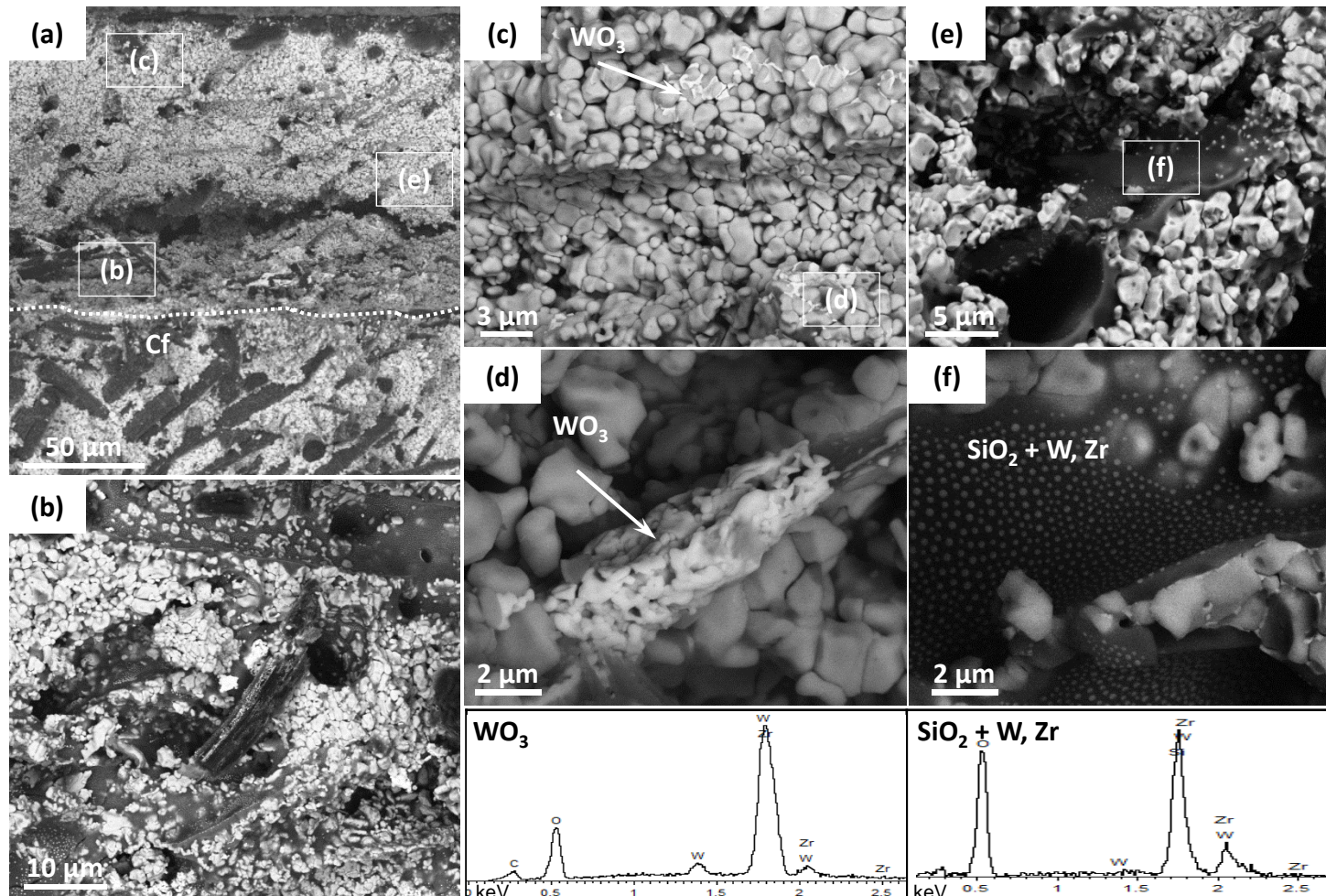
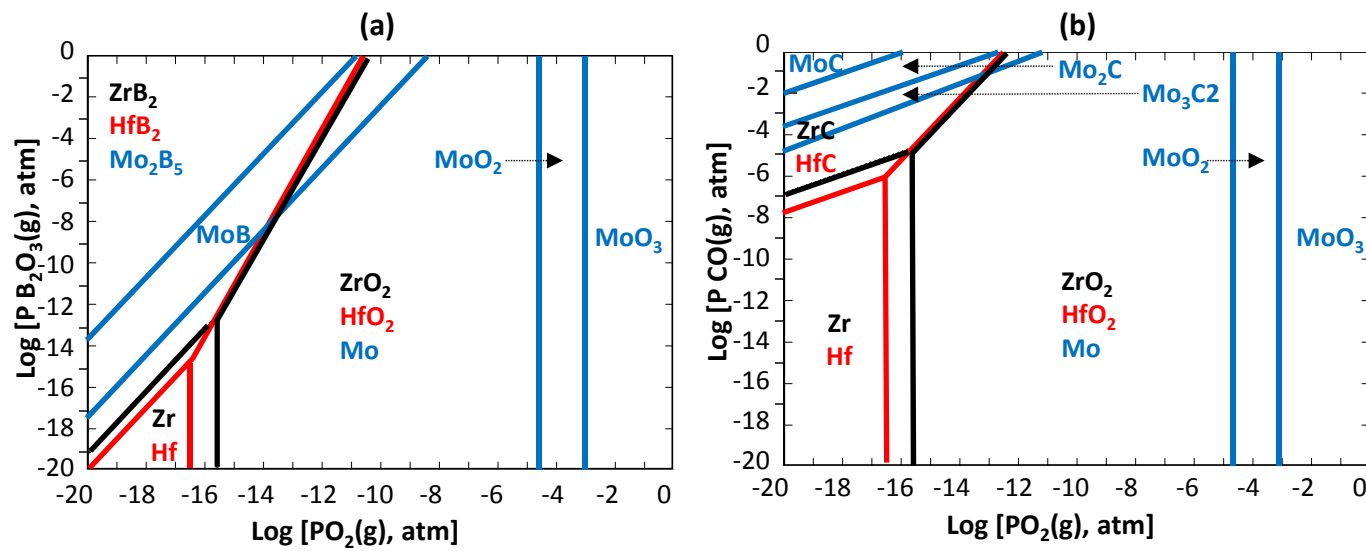


Fig. 15



Gr abstract

